



Cite this: *Dalton Trans.*, 2015, **44**, 16824

## Luminescent mononuclear mixed ligand complexes of copper(i) with 5-phenyl-2,2'-bipyridine and triphenylphosphine<sup>†‡</sup>

Damir A. Safin,<sup>\*a</sup> Mariusz P. Mitoraj,<sup>\*b</sup> Koen Robeyns,<sup>a</sup> Yaroslav Filinchuk<sup>a</sup> and Christophe M. L. Vande Velde<sup>\*c</sup>

Reaction of 5-phenyl-2,2'-bipyridine (**L**) with a mixture of CuI or [Cu(CH<sub>3</sub>CN)<sub>4</sub>]BF<sub>4</sub> and PPh<sub>3</sub> leads to mononuclear heteroleptic complexes [CuL(PPh<sub>3</sub>)I] (**1**) and [CuL(PPh<sub>3</sub>)<sub>2</sub>]BF<sub>4</sub> (**2**). According to X-ray diffraction, **L** crystallizes in the monoclinic space group *P*2<sub>1</sub>/*n*, exhibiting a disorder over four orientations. Complexes **1** and **2** crystallize in the monoclinic space groups *P*2<sub>1</sub>/*c* and *P*2<sub>1</sub>, respectively. **1** comprises a discrete neutral molecule, while **2** has an ionic structure containing [CuL(PPh<sub>3</sub>)<sub>2</sub>]<sup>+</sup> and BF<sub>4</sub><sup>-</sup>. Both structures reveal that each tetracoordinated copper(i) atom is linked to two nitrogen atoms of **L**, one iodide and one PPh<sub>3</sub> in the structure of **1**, or two PPh<sub>3</sub> in the structure of **2** with the formation of a distorted tetrahedral coordination core. The structure of **2** is additionally stabilized by a weak intramolecular  $\pi\cdots\pi$  stacking interaction formed between two adjacent phenyl rings of two PPh<sub>3</sub> ligands. Hirshfeld surface analysis showed that the structures of both complexes are mainly characterized by H $\cdots$ H and C $\cdots$ H contacts as well as by I $\cdots$ H in the structure of **1** and F $\cdots$ H in the structure of **2**. The 2D fingerprint plots of two different molecules in the structure of **L** showed that both molecules exhibit contacts for  $\pi\cdots\pi$  stacking interactions. The factors important for the stability of **1** and **2** were further quantitatively and qualitatively characterized by the charge and energy decomposition method ETS-NOCV. According to diffuse reflectance spectroscopy in the solid state, free **L** exhibits bands exclusively in the UV region, while the spectra of **1** and **2** also contain bands in the visible range up to about 500 and 600 nm. All three compounds were found to be emissive in the solid state. DFT calculations have shown that, while emission of **L** is due to the ligand-centered  $\pi \rightarrow \pi^*$  transition, luminescence of **1** and **2** was assigned to a (M + X)LCT and MLCT excited states, respectively.

Received 20th July 2015,  
Accepted 1st September 2015

DOI: 10.1039/c5dt02755a

www.rsc.org/dalton

## Introduction

Copper(i) complexes are of ever increasing interest due to their attractive photophysical properties for luminescent sensors and probes, electroluminescence, and solar energy conver-

sion.<sup>1</sup> N-heterocyclic ligands, in particular polypyridine compounds, are known to be an efficient tool to tune the luminescence properties of copper(i) complexes.<sup>2</sup> These ligands can be easily modified by introducing different substituents, possessing a variety of electronic, steric and conformational impacts on both the coordinated chelate and coordination core. Furthermore, the nature of additional ligands, in particular halides and phosphines, was found to affect the luminescence properties of copper(i) compounds.<sup>3</sup>

N-heterocyclic compounds such as 2,2'-bipyridine, 1,10-phenanthroline and 2,2':6',2''-terpyridine seem to be the most widely used polypyridine luminophore ligands for metal complexes. However, these ligands alone exhibit undesirable luminescence at short wavelengths due to the emission from the  $n\text{-}\pi^*$  excited state.<sup>4</sup> Furthermore, since the 2,2'-bipyridine framework is polarized along the 5,5'-axis,<sup>5</sup> introduction of aromatic substituents into these positions leads to an increase of the conjugation and, thus, increase of polarization along

<sup>a</sup>Institute of Condensed Matter and Nanosciences, Molecules, Solids and Reactivity (IMCN/MOST), Université catholique de Louvain, Place L. Pasteur 1, 1348 Louvain-la-Neuve, Belgium. E-mail: damir.a.safin@gmail.com

<sup>b</sup>Department of Theoretical Chemistry, Faculty of Chemistry, Jagiellonian University, R. Ingardena 3, 30-060 Cracow, Poland. E-mail: mitoraj@chemia.uj.edu.pl

<sup>c</sup>Faculty of Applied Engineering, Advanced Reactor Technology, University of Antwerp, Salesianenlaan 90, BE-2660 Hoboken, Belgium.

E-mail: christophe.vandeveld@uantwerpen.be

<sup>†</sup>Dedicated to Professor F. Ekkehardt Hahn on the Occasion of his 60th Birthday.

<sup>‡</sup>Electronic supplementary information (ESI) available: Fig. S1–S4 and Table S1. CCDC 1410040–1410042. For ESI and crystallographic data in CIF or other electronic format see DOI: 10.1039/c5dt02755a

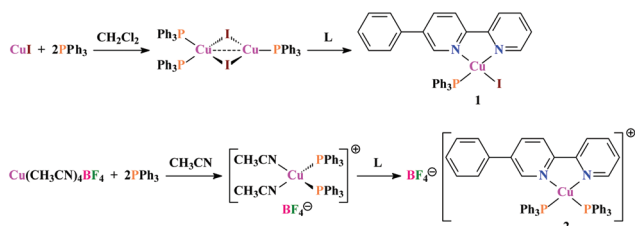
this axis. This, in turn, will lead to higher luminescence as well as to a red-shift of the emission maximum.<sup>6</sup> With this in mind, we have directed our attention to the 5-phenyl-2,2'-bipyridine (**L**), which was synthesized according to the known procedure.<sup>7</sup>

In this contribution, we describe the synthesis, complete structural investigation and solid state photophysical properties of **L** and its two novel luminescent mononuclear heteroleptic copper(I) complexes [CuL(PPh<sub>3</sub>)I] (**1**) and [CuL(PPh<sub>3</sub>)<sub>2</sub>]BF<sub>4</sub> (**2**). The experimental results were supported by detailed quantum chemical calculations.

## Results and discussion

The complexes **1** and **2** were prepared by reacting CuI or [Cu(CH<sub>3</sub>CN)<sub>4</sub>]BF<sub>4</sub>, respectively, with two equivalents of PPh<sub>3</sub>, followed by addition of one equivalent of **L** (Scheme 1). The structures of the intermediate compounds [(Ph<sub>3</sub>P)<sub>2</sub>Cu(μ-I)<sub>2</sub>Cu(PPh<sub>3</sub>)]<sup>8</sup> and [Cu(CH<sub>3</sub>CN)<sub>2</sub>(PPh<sub>3</sub>)<sub>2</sub>]BF<sub>4</sub> (ref. 9) were revealed by single crystal X-ray diffraction. The obtained orange (**1**) and yellow (**2**) solid materials are soluble in most polar solvents.

The <sup>31</sup>P{<sup>1</sup>H} NMR spectrum of **1** in DMSO-*d*<sub>6</sub> exhibits a unique sharp (FWHM = 5.2 Hz) signal at 26.0 ppm, while the <sup>31</sup>P{<sup>1</sup>H} NMR spectrum of **2** in the same solvent contains an extremely broad (FWHM = 167.5 Hz) signal at 2.6 ppm. The latter broadening can be due to a slow, in the NMR timescale, equilibrium in DMSO-*d*<sub>6</sub> between the coordinated and non-coordinated PPh<sub>3</sub> ligands in the structure of **2**. The resonances in both spectra show a downfield shift relative to free PPh<sub>3</sub>, supporting the fact that the phosphorus atoms coordinate to the metal ion. In contrast to the <sup>31</sup>P{<sup>1</sup>H} NMR spectrum of **1**, exclusively exhibiting a unique sharp signal, the <sup>1</sup>H NMR spectrum of the same complex contains two significantly broadened singlets at 8.02–9.16 and 10.62–11.64 ppm, arising from seven protons of the ligand **L**. This can be explained by a slow, in the NMR timescale, equilibrium in DMSO-*d*<sub>6</sub> between the coordinated and non-coordinated **L** in the structure of **1**. The signals for the PPh<sub>3</sub> and the remaining five protons of **L** were observed as two multiplets from 7.31 to 7.78 ppm. The <sup>1</sup>H NMR spectrum of **2** in DMSO-*d*<sub>6</sub> exhibits one multiplet and two triplets at 7.05–7.20, 7.29 and 7.40 ppm, respectively, corresponding to the PPh<sub>3</sub> protons. The protons of **L** were shown as a triplet of doublets at 8.15 ppm and three multiplets at 7.44–7.59, 8.37–8.49 and 8.61–8.73 ppm, respectively. Thus,



Scheme 1 Synthesis of **1** and **2**.

according to the <sup>31</sup>P{<sup>1</sup>H} and <sup>1</sup>H NMR spectroscopy, both complexes are dynamic in DMSO-*d*<sub>6</sub>. However, the complex **1** is dynamic with respect to **L**, while the complex **2** is dynamic with respect to PPh<sub>3</sub>.

The crystal structure of **L**, to the best of our knowledge, has not been reported so far. Furthermore, the Cambridge Structural Database<sup>10</sup> contains only four **L**-based structures.<sup>7b,11</sup> Thus, every new structure of coordination compounds of **L** is of value.

Compound **L** (Fig. 1) was refined in the monoclinic space group *P*<sub>2</sub><sub>1</sub>/*n*, containing one and a half independent molecules in the asymmetric unit. The planar molecule of **L** was found to be orientationally disordered, without significant positional disorder. The global shape of the molecules was retained and positions of the nitrogen atoms were distributed over all possible sites. All bond lengths and bond angles are typical for the pyridyl and phenyl fragments.<sup>12</sup> The dihedral angles between the planes formed by the aromatic rings in the crystal structure are less than 3.0°, making the molecules of **L** appear completely planar. The structure of **L** is stabilized by intermolecular π⋯π stacking interactions with an interplanar separation of about 3.6 Å, formed between the corresponding aromatic rings of adjacent molecules (Fig. 1). The π⋯π stacked molecules form two types of ribbon-like aggregates almost orthogonal to each other (~82.0°) along the *a* axis (Fig. 1).

According to the X-ray data, **1** and **2** crystallize in the monoclinic space groups *P*<sub>2</sub><sub>1</sub>/*c* and *P*<sub>2</sub><sub>1</sub>, respectively. Complex **1** com-

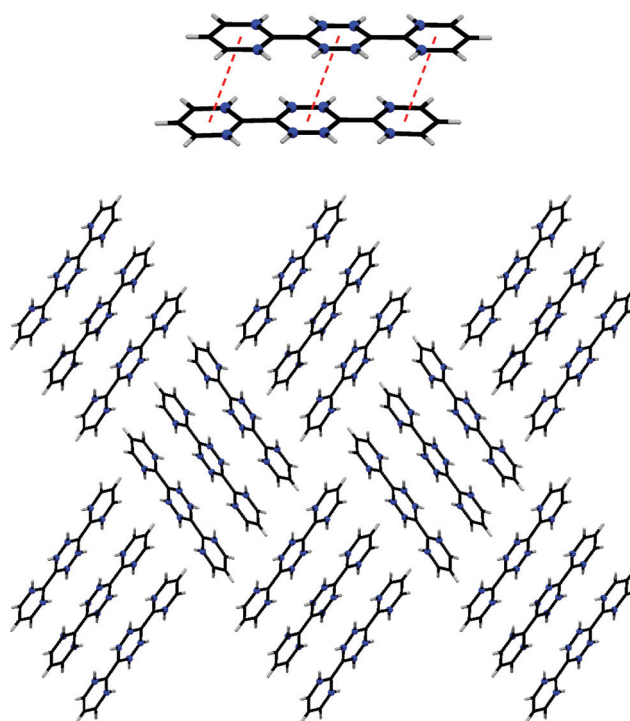


Fig. 1 Molecular structure of a π⋯π stacked dimer, constructed from two independent molecules (top), and crystal packing along the *a* axis (bottom) of **L**. Colour code: C = black, H = grey, N = blue.

prises a discrete neutral molecule, while **2** exhibits an ionic structure comprising a discrete cation  $[\text{CuL}(\text{PPh}_3)_2]^+$  and a  $\text{BF}_4^-$  anion (Fig. 2). Both structures reveal that each tetracoordinated copper(i) atom is linked to two nitrogen atoms of **L**, one iodide and one  $\text{PPh}_3$  in the structure of **1**, or two  $\text{PPh}_3$  in the structure of **2**, with the formation of a distorted tetrahedral coordination core. This distortion is due to the small bite angle of **L** (Table 1). The dihedral angles between the N–Cu–N plane and the P–Cu–I or P–Cu–P plane are about  $87.1^\circ$  and  $81.0^\circ$  for **1** and **2**, respectively. Decrease of this angle in the structure of **2** is due to repulsion between the phenyl fragments of the two  $\text{PPh}_3$  ligands. The two pyridine moieties of **L** are almost in the same plane for both complexes, which is reflected in the dihedral angles of about  $5.1^\circ$  and  $5.6^\circ$  between the two cycles (Table 1). However, the phenyl fragments deviate significantly from the pyridine planes for **1** and **2** (Fig. 2 and Table 1).

The Cu–N bond lengths in **1** are slightly longer than in **2**, while the Cu–P distance in **1** are slightly shorter than the corresponding bond lengths in **2** (Table 1). The Cu–I bond in **1**

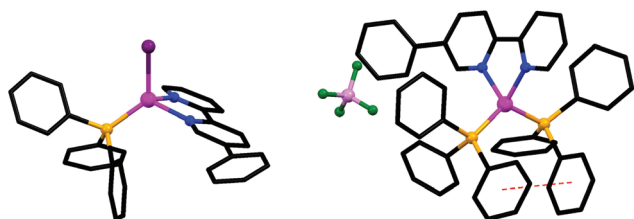


Fig. 2 Molecular structures of **1** (left) and **2** (right). Hydrogen atoms were omitted for clarity. Colour code: C = black, N = blue, B = pink, F = green, I = purple, P = orange, Cu = magenta.

Table 1 Selected bond lengths, bond and dihedral angles for **1** and **2**

	<b>1</b>		<b>2</b>	
	Experimental	DFT	Experimental	DFT
<i>Bond length (Å)</i>				
Cu–N	2.086(3)	2.11	2.062(4)	2.14
	2.092(3)	2.16	2.066(4)	
Cu–P	2.2030(9)	2.24	2.2389(13)	2.28
			2.2619(13)	2.29
Cu–I	2.5923(5)	2.67	—	—
<i>Bond angle (°)</i>				
N–Cu–N	78.74(11)	77.3	79.44(15)	77.5
N–Cu–P	115.46(8)	111.2	103.44(11)	105.7
	116.56(8)	124.0	111.95(11)	107.9
			113.14(11)	112.9
			124.45(11)	122.7
N–Cu–I	105.13(8)	110.9	—	—
	110.14(7)	116.7		
P–Cu–I	122.31(3)	111.0	—	—
P–Cu–P	—	—	118.31(5)	121.7
<i>Dihedral angle (°)</i>				
Py...Py	5.14(16)	3.2	5.6(2)	10.6
Py...Ph(L)	33.65(17)	31.3	30.0(2)	28.3
	36.83(17)		34.9(3)	

is about  $2.6 \text{ \AA}$ . The N–Cu–N angles are identical for both complexes and about  $79^\circ$ , while the N–Cu–P angles are almost the same in the structure of **1** ( $\sim 116^\circ$ ) and significantly deviate in the structure of **2** ( $\sim 103\text{--}124^\circ$ ) (Table 1).

The structure of **2** is additionally stabilized by a weak intramolecular  $\pi\cdots\pi$  stacking interaction with an interplanar separation of about  $3.9 \text{ \AA}$ , formed between two adjacent phenyl rings of two  $\text{PPh}_3$  ligands (Fig. 2). No  $\pi\cdots\pi$  stacking interactions were found in the structure of **1**.

A closer inspection of both crystal structures revealed no classical hydrogen bonds but further H...X short contacts. However, based on established criteria<sup>13</sup> these weak interactions are not directing the crystal packing or molecular structures.

The bulk samples of **L**, **1** and **2** were studied by means of X-ray powder diffraction analysis (Fig. 3). The experimental X-ray powder patterns are in agreement with the calculated powder patterns obtained from the single crystal X-ray analyses, showing that the bulk materials of **L**, **1** and **2** are free from phase impurities.

In order to examine the interactions in the crystal structures of **L**, **1** and **2**, the Hirshfeld surface analysis<sup>14</sup> and the 2D fingerprint plots<sup>15</sup> were obtained using CrystalExplorer 3.1.<sup>16</sup> Since the structure of **L** contains one and a half molecules in the asymmetric unit, two different pairs of Hirshfeld surfaces were obtained for two different molecules of **L**, namely the “first molecule” in the general position and the “second molecule” for the one on the inversion centre.

According to the Hirshfeld surface analysis, for both molecules of **L** as well as for **1** and **2**, the intermolecular H...H contacts, comprising 59.2, 57.4, 54.0 and 50.4% of the total number of contacts respectively, are major contributors to the crystal packing (Fig. 4). The shortest H...H contacts are shown in the fingerprint plots as characteristic spikes at  $d_e + d_i \approx 2.2 \text{ \AA}$  (Fig. 5, Fig. S1–S3 in the ESI†). A subtle feature is evident in the fingerprint plot for the first molecule of **L** and it was also less visible in the corresponding plots of the second mole-

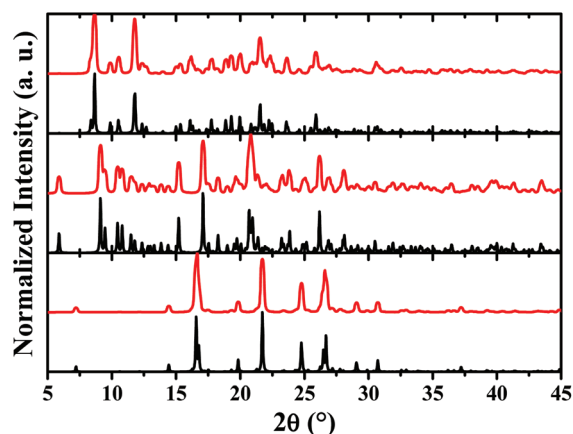


Fig. 3 Calculated (black) and experimental (red) X-ray powder diffraction patterns of **L** (bottom), **1** (middle) and **2** (top).

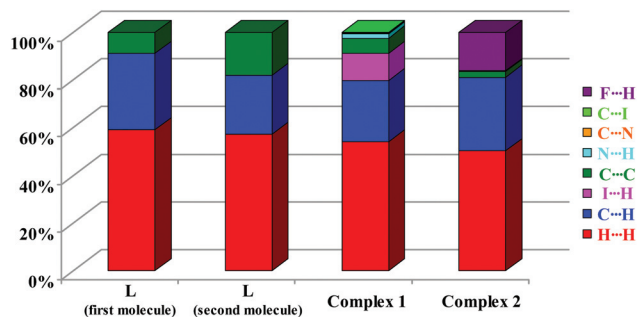


Fig. 4 Relative contributions of intermolecular contacts to the Hirshfeld surface area in the first and second molecules of L, 1 and 2.

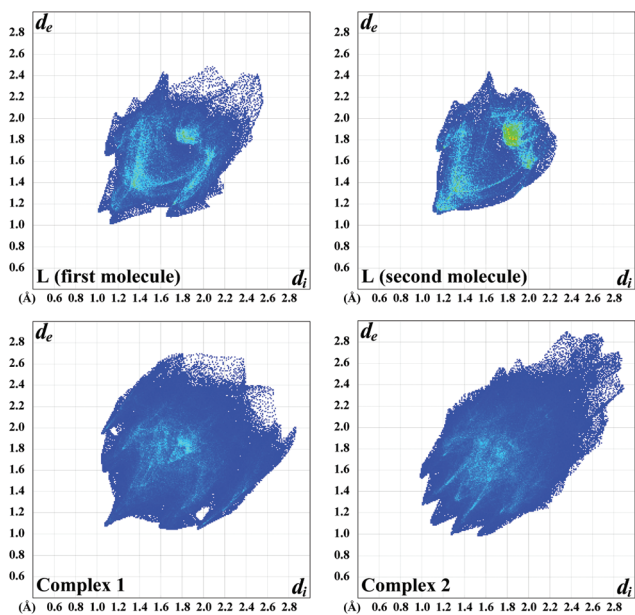


Fig. 5 2D fingerprint plots of observed contacts for the first (top row, left) and second (top row, right) molecules of L (top), and for 1 (bottom row, left) and 2 (bottom row, right).

molecule of L and 2. In each of these cases there is a distinct splitting of the short H...H fingerprint. This splitting occurs when the shortest contact is between three atoms, rather than for a direct two-atom contact.<sup>15</sup>

The structures of both molecules of L and both complexes are also dominated by C...H contacts, comprising 31.9, 24.5, 25.7 and 30.7% (Fig. 4), respectively, of the total Hirshfeld surface areas (Fig. 5, Fig. S1–S3 in the ESI†). It should be noted that the first molecule of L exhibits a much larger proportion of C...H contacts than the second molecule of L. These contacts in the fingerprint plot of 1 are shown in the form of clearly pronounced “wings” with the shortest  $d_e + d_i \approx 2.6$  Å (Fig. 5, Fig. S2 in the ESI†), which are recognized as characteristic of a C–H... $\pi$  interaction.<sup>15</sup> The first molecule of L exhibits similar “wings” due to C–H... $\pi$  interactions (Fig. 5, Fig. S1 in the ESI†). However, the latter plot contains one more C–H... $\pi$

interaction and, as a result, the distinct sawtooth shape on the upper left and lower right of the plot is observed (Fig. 5, Fig. S1 in the ESI†).

It is worth adding that the fingerprint plot of the first molecule of L exhibits a significant number of points at large  $d_e$  and  $d_i$ , shown as tails at the top right of the plot, when compared to the plot of the second molecule of L (Fig. 5, Fig. S1 in the ESI†). These points, similar to those observed in the fingerprint plot of benzene,<sup>15</sup> correspond to regions on the Hirshfeld surface without any close contacts to nuclei in adjacent molecules.

The structure of the second molecule of L is further characterized by a significant proportion of C...C contacts, comprising 18.1%, while a lower proportion (8.9%) of the same contacts were found in the first molecule of L (Fig. 4). They are shown on the fingerplots as the areas of pale blue/green color, and even mixed with yellow and red points on the plot of the second molecule of L, on the diagonal at  $d_e = d_i \approx 1.7$ – $1.8$  Å (Fig. 5, Fig. S1 in the ESI†). These contacts correspond to the presence of  $\pi$ ... $\pi$  stacking interactions in the crystal structure of L. These interactions are also featured on the fingerplots of both complexes (Fig. 5, Fig. S2 and S3 in the ESI†). However, minor areas (6.5 and 2.5% in 1 and 2, respectively) (Fig. 4) of pale blue color are present.

Another significant contribution (16.3%) on the total Hirshfeld surface area of 2 arises from F...H contacts (Fig. 4) with the shortest  $d_e + d_i \approx 2.3$  Å (Fig. 5, Fig. S3 in the ESI†). Close inspection of other intermolecular contacts also revealed a negligible proportion of N...H (1.7%), C...N (0.4%) and C...I (0.4%) contacts in the structure of 1 (Fig. 5, Fig. S2 in the ESI†), and N...H (0.1%) contacts in the structure of 2 (Fig. 5, Fig. S3 in the ESI†). No other contacts were found in the structures of both molecules of L and both complexes.

To establish the origin of the different colors of L (colorless), 1 (orange) and 2 (yellow) as well as to study their electronic properties, diffuse reflectance spectra were recorded on pure samples (Fig. 6). The spectrum of L exhibits a broad band

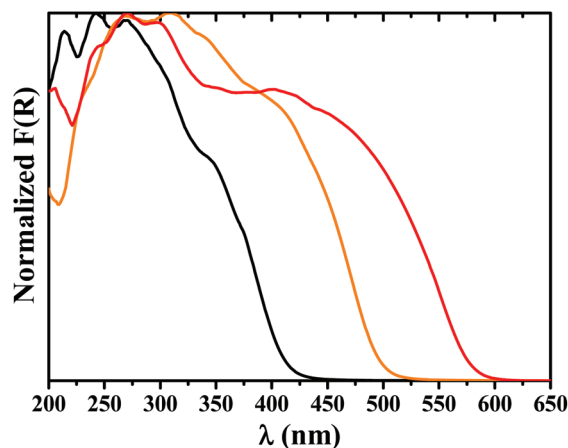


Fig. 6 Normalized Kubelka–Munk spectra of L (black), 1 (red) and 2 (orange) at 298 K.

with several maxima exclusively in the UV region corresponding to intra-ligand  $\pi \rightarrow \pi^*$  transitions. The spectra of the complexes exhibit a broad band with several maxima in the range of 200 to 600 or 500 nm for **1** and **2**, respectively. While the bands in the UV region are coming from intra-ligand  $\pi \rightarrow \pi^*$  transitions of **L** and  $\text{PPh}_3$ , the bands in the visible range are assigned to a metal-to-ligand charge transfer (MLCT) transition from the  $d\pi$  orbital of the  $3d^{10}$  copper(I) center to the unoccupied  $\pi^*$  orbital of the ligand **L**. This transition in **1** is further mixed with a halide-to-ligand charge transfer (XLCT) transition. The (M + X)LCT transition is significantly red-shifted in the spectrum of **1** compared to the MLCT transition in the spectrum of **2**. This can be explained by lowering of the highest occupied molecular orbitals (HOMO) energy upon coordination of two  $\pi$ -acceptor  $\text{PPh}_3$  ligands in the structure of **2**, compared to one  $\text{PPh}_3$  ligand in the structure of **1**, hence increasing the energy gap between the HOMO and the lowest unoccupied molecular orbitals (LUMO).

The emission spectrum of **L** exhibits a single intense band centred at 395 nm (Fig. 7), which was assigned to the fluorescence emission from ligand-centered  $\pi \rightarrow \pi^*$  transition. This was supported by the excitation spectrum, which reveals a main contribution from the band centred at 350 nm (Fig. 7).

Surprisingly, the fluorescence spectrum of the iodide complex **1** shows two bands centered at about 420 and 630 nm upon excitation at  $\lambda_{\text{exc}} = 360$  nm (Fig. 8). The high energy emission band is obviously due to the fluorescence emission from ligand-centered  $\pi \rightarrow \pi^*$  transition of **L**, which is revealed from the excitation spectrum of **1** measured at  $\lambda_{\text{em}} = 425$ . This is further supported by comparison with the emission spectrum of free **L** (Fig. 7). The latter red-shifted emission band in the spectrum of **1** can be isolated upon excitation with visible light at  $\lambda_{\text{exc}} = 525$  nm. This emission can be assigned to the mixed (M + X)LCT excited state.

Complex **2** exhibits an intense emission band centered at about 575 nm (Fig. 9). Notably, no other emission bands were observed in the fluorescence spectrum of **2** regardless of the

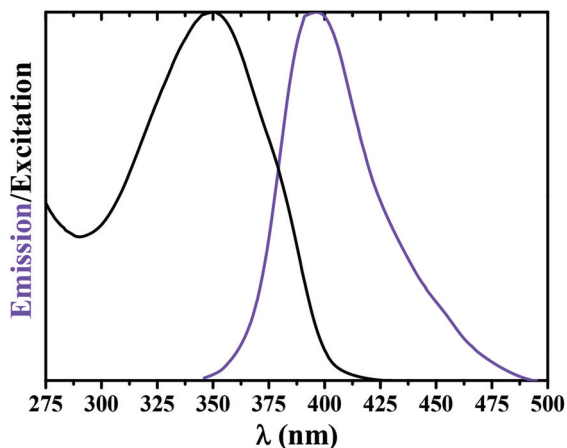


Fig. 7 Normalized solid-state emission (violet,  $\lambda_{\text{exc}} = 340$  nm) and excitation (black,  $\lambda_{\text{em}} = 400$  nm) spectra of **L** at 298 K.

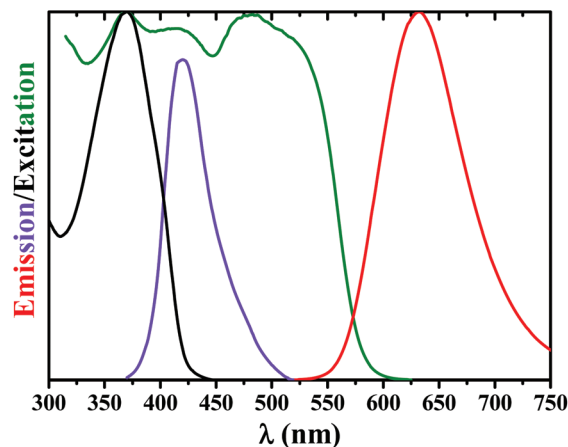


Fig. 8 Normalized solid-state emission (violet,  $\lambda_{\text{exc}} = 360$ ; and red,  $\lambda_{\text{exc}} = 525$ ) and excitation (black,  $\lambda_{\text{em}} = 425$ ; and green,  $\lambda_{\text{em}} = 620$ ) spectra of **1** at 298 K.

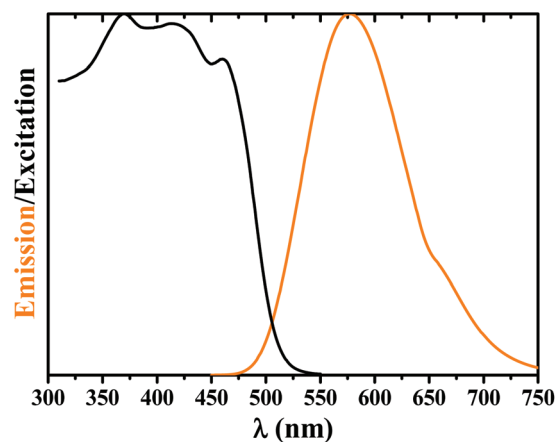


Fig. 9 Normalized solid-state emission (orange,  $\lambda_{\text{exc}} = 425$  nm) and excitation (black,  $\lambda_{\text{em}} = 580$  nm) spectra of **2** at 298 K.

excitation wavelength. The observed emission is about 55 nm blue-shifted relative to the low energy emission band in the spectrum of **1** (Fig. 8). This, obviously, can be explained by the replacement of iodide by an efficient  $\pi$ -acceptor  $\text{PPh}_3$ . This, in turn, leads to a lowering of the HOMO level and, thus, to a larger HOMO–LUMO gap.

For **1** and **2**, the HOMO is distributed over either the copper(I) and iodide ions in **1** or the copper(I) ion alone in **2** with some contribution from the  $\text{PPh}_3$  ligands. However, the LUMO for both complexes is mainly on the ligand **L**.<sup>1</sup> The presence of another  $\text{PPh}_3$  in **2** would have an insignificant influence on the LUMO level. Thus, the corresponding emission states at 630 and 575 nm in the fluorescence spectra of **1** and **2** can be assigned to (M + X)LCT and MLCT excited states, respectively.

In order to further characterize complexes **1** and **2** we have performed geometry optimization based on DFT/TZP/BLYP-D3 by means of the Amsterdam Density Functional package.<sup>17</sup>

The calculated parameters of the optimized structures of **1** and **2** are in agreement with the experimental results (Table 1). Furthermore, the calculated HOMO–LUMO gap for **2** is 0.882 eV larger in comparison with that of **1** (Fig. 10). This is fully consistent with the experimental blue-shift of the emission band in the spectrum of **2** (Fig. 9) compared with the spectrum of **1** (Fig. 8). The HOMO of **1** is built from the lone electron pair of iodine supported by the copper d orbital, whereas the empty  $\pi^*$ (LUMO) is located entirely on **L**. Some contributions from the lone electron pairs of the phosphorus and nitrogen atoms are also visible in the shape of HOMO. Similar molecular orbital characteristics are valid for **2**. However, the HOMO comprises a more significant contribution from the lone electron pairs of the phosphorus atom (Fig. 10). This confirms that luminescence of **1** and **2** originate from the (M + X)LCT and MLCT charge transfers, respectively.

We have further shed some light on factors that influence the stability of **1** and **2** by detailed analysis of the Cu–P bonds by the means of the charge and energy decomposition method ETS-NOCV.<sup>18</sup> In **1**, the interaction between two neutral fragments, PPh<sub>3</sub> and [CuLI], was considered, while in **2**, PPh<sub>3</sub> interacts with the cationic fragment [CuLPPh<sub>3</sub>]<sup>+</sup> (Table S1 in the ESI<sup>†</sup>). Similarly, bonding between **L** and [CuPPh<sub>3</sub>I] or [Cu(PPh<sub>3</sub>)<sub>2</sub>]<sup>+</sup> in **1** and **2**, respectively, were also characterized (Table S1 in the ESI<sup>†</sup>).

It was found, that the overall interaction energy ( $\Delta E_{\text{int}}$ ) of [CuLPPh<sub>3</sub>]<sup>+</sup>–PPh<sub>3</sub> in **2** is significantly lower in comparison with that of [CuLI]–PPh<sub>3</sub> in **1** (Table S1 in the ESI<sup>†</sup>). Decomposition of  $\Delta E_{\text{int}}$  into the specific components allows to conclude that it is predominantly due to the weaker steric repulsion (measured by  $\Delta E_{\text{Pauli}}$ ) as well as more significant dispersion ( $\Delta E_{\text{disp}}$ ) contribution due to  $\pi \cdots \pi$  stacking between the phenyl rings (Table S1 in the ESI<sup>†</sup>). The orbital interaction term ( $\Delta E_{\text{orb}}$ ) is of the same importance for both [CuLPPh<sub>3</sub>]<sup>+</sup>–PPh<sub>3</sub> in **2** and [CuLI]–PPh<sub>3</sub> in **1**. Apart from the dominant dative contributions to the [CuLPPh<sub>3</sub>]<sup>+</sup>–PPh<sub>3</sub> bond in **2**, described by  $\Delta\rho_1$

(donation from the lone pair of phosphorus to copper) and back-donations ( $\Delta\rho_2$ ,  $\Delta\rho_3$ ) from the occupied d orbital of copper(i) to  $\sigma^*$ (P–C), one can clearly see polarizations of the phenyl rings due to the non-covalent  $\pi \cdots \pi$  interactions ( $\Delta\rho_3$ ,  $\Delta\rho_4$  and  $\Delta\rho_5$  in Fig. S4 in the ESI<sup>†</sup>). It should be noted that a significant role of the dispersion for the stabilization of **2** is also visible when comparing [CuPPh<sub>3</sub>I]–**L** in **1** with [Cu(PPh<sub>3</sub>)<sub>2</sub>]<sup>+</sup>–**L** in **2** (Table S1 in the ESI<sup>†</sup>). Finally, it can be noted that the [CuLPPh<sub>3</sub>]<sup>+</sup>–PPh<sub>3</sub> bond in **2** is weaker compared with the [Cu(PPh<sub>3</sub>)<sub>2</sub>]<sup>+</sup>–**L** bond. This qualitatively explains why **2** is in equilibrium with PPh<sub>3</sub> but not with **L** in solution. The  $\Delta E_{\text{int}}$  values of [CuLI]–PPh<sub>3</sub> and [CuPPh<sub>3</sub>I]–**L** in **1** are almost the same (Table S1 in the ESI<sup>†</sup>). Accordingly, the feasibility of dissociation of **L** over PPh<sub>3</sub> in **1** observed from NMR should rather be related to other factors including, *e.g.*, interactions with the solvent.

Finally, we have also complemented the Hirshfeld surface analysis by the detailed ETS-NOCV-based calculations of intermolecular interactions in **1** and **2** with the geometries as in the crystals (Fig. 11). It was established, that the dispersion contribution ( $\Delta E_{\text{disp}}$ ) is the most important for the overall stabilization of **1**, while the electrostatic ( $\Delta E_{\text{elstat}}$ ) and orbital ( $\Delta E_{\text{orb}}$ ) interaction terms are less significant (Fig. 11). Furthermore, the deformation density ( $\Delta\rho_{\text{orb}}$ ), corresponding to  $\Delta E_{\text{orb}}$ , clearly displays the formation of the intermolecular C–H $\cdots$ I and C–H $\cdots$ H–C contacts (Fig. 11). On the other hand, similar analysis performed for **2** leads to the conclusion that the most crucial stabilizing factor is the electrostatic ( $\Delta E_{\text{elstat}}$ ) stabilization. It proves a significant ionicity. The dispersion ( $\Delta E_{\text{disp}}$ ) term is the least important. The charge-transfer orbital interaction contribution ( $\Delta E_{\text{orb}}$ ) describes predominantly the formation of the C–H $\cdots$ F contacts (Fig. 11).

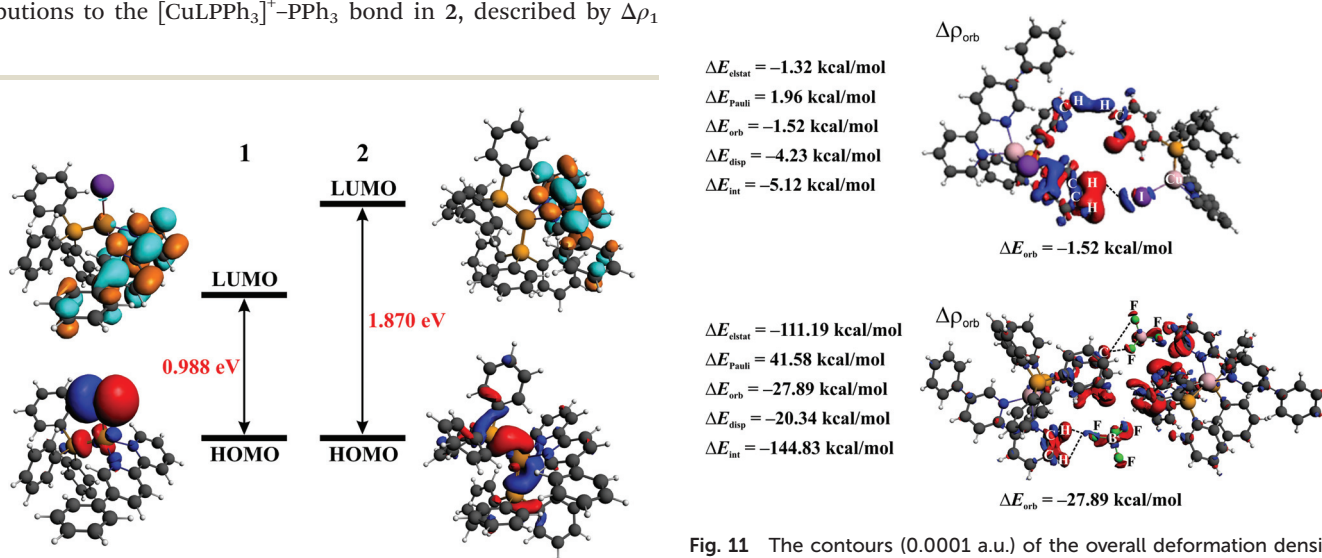


**Fig. 10** The contours of molecular orbitals (0.03 a.u.) and the HOMO–LUMO gaps, obtained from the DFT/TZP/BLYP-D3 calculations, for **1** (left) and [CuL(PPh<sub>3</sub>)<sub>2</sub>]<sup>+</sup> in **2** (right).

**Fig. 11** The contours (0.0001 a.u.) of the overall deformation densities ( $\Delta\rho_{\text{orb}}$ ) together with the corresponding orbital interaction energies ( $\Delta E_{\text{orb}}$ ), describing the interaction between two monomers in **1** (top) and **2** (bottom). Red color shows charge depletion, whereas the blue color indicates charge accumulation due to bond formation.

## Conclusions

We have synthesised two mononuclear heteroleptic copper(I) complexes,  $[\text{CuL}(\text{PPh}_3)\text{I}]$  (**1**) and  $[\text{CuL}(\text{PPh}_3)_2]\text{BF}_4$  (**2**), with 5-phenyl-2,2'-bipyridine (**L**) and  $\text{PPh}_3$ , using two different metal sources, namely  $\text{CuI}$  and  $[\text{Cu}(\text{CH}_3\text{CN})_4]\text{BF}_4$ . The different nature of the iodide and tetrafluoroborate ions, which are coordinating and non-coordinating ligands respectively, allowed to control the coordination core of the complexes. According to X-ray structure determination, complex **1** was obtained as a discrete neutral molecule, while **2** exhibits an ionic structure comprising a discrete cation  $[\text{CuL}(\text{PPh}_3)_2]^+$  and a  $\text{BF}_4^-$  counterion. Furthermore, the crystal structure of **L** was established for the first time. NMR spectroscopy revealed that **1** is dynamic with respect to **L**, while **2** is dynamic with respect to  $\text{PPh}_3$  in  $\text{DMSO}-d_6$ .

According to the Hirshfeld surface analysis, it was found that the structures of both complexes are mainly characterized by  $\text{H}\cdots\text{H}$  and  $\text{C}\cdots\text{H}$  intermolecular contacts as well as by  $\text{I}\cdots\text{H}$  in the structure of **1** and  $\text{F}\cdots\text{H}$  in the structure of **2**. Although the decomposed 2D fingerprint plots of two different molecules in the structure of **L** show a very similar major contribution from  $\text{H}\cdots\text{H}$  intermolecular contacts, proportions of the remaining  $\text{C}\cdots\text{H}$  and  $\text{C}\cdots\text{C}$  contacts differ significantly. The  $\text{C}\cdots\text{H}$  contacts for one of the two independent molecules of **L** were found mainly in the form of  $\text{C}-\text{H}\cdots\pi$  interactions. Both independent molecules in the structure of **L** exhibit contacts for  $\pi\cdots\pi$  stacking interactions, which are more pronounced for the second molecule.

The optical and luminescence properties of **L**, **1** and **2** in the solid state at ambient temperature were also studied. According to diffuse reflectance spectroscopy, free **L** exhibits bands exclusively in the UV region, while the spectra of **1** and **2** also contain bands in the visible range up to about 500 and 600 nm. This explains why **L** is colorless, while **1** and **2** are orange and yellow, respectively. All three compounds were found to be emissive in the solid state. DFT calculations allowed to describe the molecular orbitals involved in the transitions upon excitation. While emission of **L** is due to the ligand-centered  $\pi \rightarrow \pi^*$  transition, luminescence of **1** and **2** was assigned to  $(\text{M} + \text{X})\text{LCT}$  and  $\text{MLCT}$  excited states, respectively.

## Experimental

### General procedures

NMR spectra in  $\text{DMSO}-d_6$  were obtained on a Bruker Avance 300 MHz spectrometer at 25 °C.  $^1\text{H}$  and  $^{31}\text{P}\{^1\text{H}\}$  NMR spectra were recorded at 299.948, and 121.420 MHz, respectively. Chemical shifts are reported with reference to  $\text{SiMe}_4$  ( $^1\text{H}$ ) and 85%  $\text{H}_3\text{PO}_4$  ( $^{31}\text{P}\{^1\text{H}\}$ ). Diffuse reflectance spectra were obtained with a Varian Cary 5E spectrometer using polytetrafluoroethylene (PTFE) as a reference. Spectra were measured on pure solids. Eventual distortions in the Kubelka–Munk spectra that could result from the study of pure compounds have not been considered because no comparison with absorption spectra

was necessary. Solid-state emission spectra were obtained with a Fluorolog-3 (Jobin-Yvon-Spex Company) spectrometer. Kubelka–Munk and emissions spectra were normalized to allow meaningful comparisons. Elemental analyses were performed on a Thermoquest Flash EA 1112 Analyzer from CE Instruments.

### DFT calculations

We have used the ADF2012.01 program<sup>17</sup> based on DFT/BLYP-D3/TZP. The charge and energy decomposition scheme ETS-NOCV<sup>18</sup> was applied to describe the bonding situation.

### Synthesis of **1** and **2**

A solution of **L** (0.1 mmol, 23.2 mg) in  $\text{CH}_2\text{Cl}_2$  for **1** or  $\text{CH}_3\text{CN}$  for **2** (5 mL) was added dropwise under vigorous stirring to a mixture of  $\text{CuI}$  (0.1 mmol, 19.0 mg) and  $\text{PPh}_3$  (0.2 mmol, 52.5 mg) in  $\text{CH}_2\text{Cl}_2$  (10 mL) for **1** or a mixture of  $[\text{Cu}(\text{CH}_3\text{CN})_4]\text{BF}_4$  (0.1 mmol, 31.5 mg) and  $\text{PPh}_3$  (0.2 mmol, 52.5 mg) in  $\text{CH}_3\text{CN}$  for **2** (10 mL). The mixture was stirred at room temperature for 1 h. The solvent was then removed *in vacuo*. Complexes were isolated by recrystallisation from a 1 : 4 mixture of  $\text{CH}_2\text{Cl}_2$  and *n*-hexane.

1. Orange crystals. Yield: 64.4 mg (94%).  $^1\text{H}$  NMR,  $\delta$ : 7.31–7.48 (m, 6H, *o*-H,  $\text{PPh}_3$ ), 7.49–7.78 (m, 15H, *m*-H + *p*-H,  $\text{PPh}_3$ ; **L**), 8.02–9.16 (br. s, 5H, **L**), 10.62–11.64 (br. s, 2H, **L**) ppm.  $^{31}\text{P}\{^1\text{H}\}$  NMR,  $\delta$ : 26.0 (s) ppm. Anal. Calc. for  $\text{C}_{34}\text{H}_{27}\text{CuIN}_2\text{P}$  (685.03): C 59.61, H 3.97, N 4.09. Found: C 59.52, H 4.03, N 4.06%.

2. Yellow crystals. Yield: 78.9 mg (87%).  $^1\text{H}$  NMR,  $\delta$ : 7.05–7.20 (m, 12H, *o*-H,  $\text{PPh}_3$ ), 7.29 (t,  $^3J_{\text{H,H}} = 7.3$  Hz, 12H, *m*-H,  $\text{PPh}_3$ ), 7.40 (t,  $^3J_{\text{H,H}} = 7.3$  Hz, 6H, *p*-H,  $\text{PPh}_3$ ), 7.44–7.59 (m, 6H, **L**), 8.15 (t. d,  $^3J_{\text{H,H}} = 7.8$  Hz,  $^4J_{\text{H,H}} = 1.3$  Hz, 1H, **L**), 8.37–8.49 (m, 2H, **L**), 8.61–8.73 (m, 3H, **L**) ppm.  $^{31}\text{P}\{^1\text{H}\}$  NMR,  $\delta$ : 2.6 (br. s) ppm. Anal. Calc. for  $\text{C}_{52}\text{H}_{42}\text{BCuF}_4\text{N}_2\text{P}_2$  (907.22): C 68.84, H 4.67, N 3.09. Found: C 68.93, H 4.71, N 3.12%.

### X-Ray powder diffraction

X-Ray powder diffraction for bulk samples was carried out using a Rigaku Ultima IV X-ray powder diffractometer. The Parallel Beam mode was used to collect the data ( $\lambda = 1.541836$  Å).

### Single crystal X-ray diffraction

The X-ray data of **L** were collected at 100(2) K on a Bruker platform goniometer with Smart 1000 detector, using  $\text{Mo}-\text{K}\alpha$  radiation (graphite monochromated sealed tube). Diffraction images were integrated by SAINT v7.66A, and treated for absorption by SADABS.<sup>19</sup> The structure of **L** was solved by SHELXD<sup>20</sup> and refined by full-matrix least squares on  $|F^2|$  with SHELX-2014<sup>21</sup> and shelXle.<sup>22</sup> Non-hydrogen atoms were anisotropically refined and hydrogen atoms were placed on calculated positions in riding mode with temperature factors fixed at 1.2 times  $U_{\text{eq}}$  of the parent atoms.

The asymmetric unit of **L** consists of 1.5 ligand molecules, one being found on an inversion center, amounting to 6 molecules in the unit cell. Although the global outline of the perfectly flat molecule was clearly visible after the structure

solution, the structure is orientationally disordered, with the N-atoms distributed over all possible sites. **L** can adopt a *cis*- or *trans*-conformation and in combination with a pseudo-2-fold axis/pseudo-inversion center this results in 8 possible sites for the N-atoms of the molecule found on a general position. These 8 sites are refined as mixed, N or C, with both atoms of each N/C pair constrained to occupy the same position with the same thermal ellipsoids. Linear restraints are set up to ensure the correct chemical composition. For the molecule found on the inversion center a similar procedure was applied, with the linear restraints adapted in accordance to the symmetry restraints imposed by the inversion center. From the refined occupancy factors it was found that the conformations with the N-atoms in a *trans*-configuration are most abundantly present (Fig. 12).

The X-ray data for **1** and **2** were collected at 150(2) K on a Mar345 image plate detector using Mo-K $\alpha$  radiation (Xenocs Fox3D mirror). The data were integrated with the CrysAlisPro software.<sup>23</sup> The implemented empirical absorption correction was applied. The structures of **1** and **2** were solved by SHELXS<sup>20</sup> and refined by full-matrix least squares on  $|F^2|$ , using SHELXL2014/7.<sup>21</sup> Non-hydrogen atoms were anisotropically refined and the hydrogen atoms were placed on calculated positions in riding mode with temperature factors fixed at 1.2 times  $U_{eq}$  of the parent atoms.

Figures were generated using the program Mercury.<sup>24</sup>

**Crystal data for L.** C<sub>16</sub>H<sub>12</sub>N<sub>2</sub>, C<sub>8</sub>H<sub>6</sub>N;  $M_r = 348.42$  g mol<sup>-1</sup>, monoclinic, space group  $P2_1/n$ ,  $a = 5.6180(10)$ ,  $b = 15.682(3)$ ,  $c = 19.716(3)$  Å,  $\beta = 91.990(2)^\circ$ ,  $V = 1736.0(5)$  Å<sup>3</sup>,  $Z = 4$ ,  $\rho = 1.333$  g cm<sup>-3</sup>,  $\mu(\text{Mo-K}\alpha) = 0.080$  mm<sup>-1</sup>, reflections: 20 335 collected, 5657 unique,  $R_{int} = 0.021$ ,  $R_1(\text{all}) = 0.0801$ ,  $wR_2(\text{all}) = 0.1789$ .

**Crystal data for 1.** C<sub>34</sub>H<sub>27</sub>CuIN<sub>2</sub>P,  $M_r = 684.98$  g mol<sup>-1</sup>, monoclinic, space group  $P2_1/c$ ,  $a = 9.3666(3)$ ,  $b = 10.2614(3)$ ,  $c = 30.1047(11)$  Å,  $\beta = 93.907(3)^\circ$ ,  $V = 2886.76(16)$  Å<sup>3</sup>,  $Z = 4$ ,  $\rho = 1.576$  g cm<sup>-3</sup>,  $\mu(\text{Mo-K}\alpha) = 1.908$  mm<sup>-1</sup>, reflections: 19 042 collected, 5202 unique,  $R_{int} = 0.0491$ ,  $R_1(\text{all}) = 0.0417$ ,  $wR_2(\text{all}) = 0.0824$ .

**Crystal data for 2.** C<sub>52</sub>H<sub>42</sub>CuN<sub>2</sub>P<sub>2</sub>, BF<sub>4</sub>;  $M_r = 907.16$  g mol<sup>-1</sup>, monoclinic, space group  $P2_1$ ,  $a = 10.5921(4)$ ,  $b = 13.9695(6)$ ,  $c = 15.0293(5)$  Å,  $\beta = 94.299(3)^\circ$ ,  $V = 2217.58(15)$  Å<sup>3</sup>,  $Z = 2$ ,  $\rho = 1.359$  g cm<sup>-3</sup>,  $\mu(\text{Mo-K}\alpha) = 0.620$  mm<sup>-1</sup>, reflections: 16 183 collected, 8086 unique,  $R_{int} = 0.0406$ ,  $R_1(\text{all}) = 0.0437$ ,  $wR_2(\text{all}) = 0.0913$ .

CCDC 1410040 (**L**), 1410041 (**1**) and 1410042 (**2**) contain the supplementary crystallographic data.

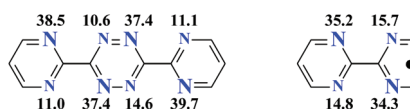


**Fig. 12** Schematic view of the asymmetric unit of **L** with possible N-atom sites shown with their occupancies (%). The major sites are shown with larger atom labels.

## Acknowledgements

The Bruker X-ray diffractometer was funded by NSF grant 0087210, Ohio Board of Regents Grant CAP-491, and by Youngstown State University. The authors thank Dr. Matthias Zeller (Youngstown State University) for collecting the data set of **L**. D. A. Safin thanks WBI (Belgium) for the post-doctoral position. This work was partly supported by FNRS.

## Notes and references

- (a) D. R. McMillin and K. M. McNett, *Chem. Rev.*, 1998, **98**, 1201; (b) P. C. Ford, E. Cariati and J. Bourassa, *Chem. Rev.*, 1999, **99**, 3625; (c) N. Armaroli, G. Accorsi, F. Cardinali and A. Listorti, *Top. Curr. Chem.*, 2007, **280**, 69; (d) Z. Liu, W. He and Z. Guo, *Chem. Soc. Rev.*, 2013, **42**, 1568; (e) Z. Liu, W. Qi and G. Xu, *Chem. Soc. Rev.*, 2015, **44**, 3117.
- (a) V. W. W. Yam and K. K. W. Lo, *Chem. Soc. Rev.*, 1999, **28**, 323; (b) Q. Zhang, Q. Zhou, Y. Cheng, L. Wang, D. Ma, X. Jing and F. Wang, *Adv. Mater.*, 2004, **16**, 432; (c) N. Armaroli, G. Accorsi, M. Holler, O. Moudam, J.-F. Nierengarten, Z. Zhou, R. T. Wegh and R. Welter, *Adv. Mater.*, 2006, **18**, 1313; (d) M. Nishikawa, K. Nomoto, S. Kume, K. Inoue, M. Sakai, M. Fujii and H. Nishihara, *J. Am. Chem. Soc.*, 2010, **132**, 9579.
- (a) D. G. Cuttall, S. M. Kuang, P. E. Fanwick, D. R. McMillin and R. A. Walton, *J. Am. Chem. Soc.*, 2002, **124**, 6; (b) M. G. Babashkina, D. A. Safin, M. Bolte and A. Klein, *CrystEngComm*, 2009, **12**, 134; (c) C. S. Smith, C. W. Branham, B. J. Marquardt and K. R. Mann, *J. Am. Chem. Soc.*, 2010, **132**, 14079; (d) D. A. Safin, M. G. Babashkina, M. Bolte and A. Klein, *Inorg. Chim. Acta*, 2010, **363**, 1897; (e) M. G. Babashkina, D. A. Safin, A. Klein and M. Bolte, *Eur. J. Inorg. Chem.*, 2010, 4018; (f) D. A. Safin, M. G. Babashkina and A. Klein, *Croat. Chem. Acta*, 2010, **83**, 353; (g) D. A. Safin, M. G. Babashkina, M. Bolte and A. Klein, *CrystEngComm*, 2011, **13**, 568; (h) D. A. Safin, M. G. Babashkina, M. Bolte and M. Köckerling, *Inorg. Chim. Acta*, 2011, **370**, 59; (i) M. G. Babashkina, D. A. Safin and Y. Garcia, *Polyhedron*, 2012, **33**, 114.
- (a) J. Kotlicka and Z. R. Grabowski, *J. Photochem.*, 1979, 413; (b) G. Albano, V. Balzani, E. C. Constable, M. Maestri and D. R. Smith, *Inorg. Chim. Acta*, 1998, **277**, 225.
- B. Bosnich, *Acc. Chem. Res.*, 1969, **2**, 266.
- J. C. Loren and J. S. Siegel, *Angew. Chem., Int. Ed.*, 2001, **40**, 754.
- (a) V. N. Kozhevnikov, D. N. Kozhevnikov, O. V. Shabunina, V. L. Rusinov and O. N. Chupakhin, *Tetrahedron Lett.*, 2005, **46**, 1791; (b) D. N. Kozhevnikov, O. V. Shabunina, D. S. Kopchuk, P. A. Slepukhin and V. N. Kozhevnikov, *Tetrahedron Lett.*, 2006, **47**, 7025.
- (a) P. G. Eller, G. J. Kubas and R. R. Ryan, *Inorg. Chem.*, 1977, **16**, 2454; (b) K. Paizanos, D. Charalampou, N. Kourkoumelis, D. Kalpogiannaki, L. Hadjirapoglou,

- A. Spanopoulou, K. Lazarou, M. J. Manos, A. J. Tasiopoulos, M. Kubicki and S. K. Hadjikakou, *Inorg. Chem.*, 2012, **51**, 12248.
- 9 J. Green, E. Sinn, S. Woodward and R. Butcher, *Polyhedron*, 1993, **12**, 991.
- 10 CSD version 5.35 (Update February 2015).
- 11 (a) A. Tian, Z. Han, J. Peng, B. Dong, J. Sha and B. Li, *J. Mol. Struct.*, 2007, **832**, 117; (b) A.-X. Tian, Z.-G. Han, J. Peng, J.-L. Zhai, B.-X. Dong and J.-Q. Sha, *J. Coord. Chem.*, 2007, **60**, 1645; (c) S. Cui, M. Zuo, J. Zhang, Y. Zhao, R. Tan, S. Liu and S. Su, *Acta Crystallogr., Sect. E: Struct. Rep. Online*, 2011, **67**, m1706; (d) S. Cui, M. Zuo, J. Zhang, Y. Zhao and H. Wang, *Acta Crystallogr., Sect. E: Struct. Rep. Online*, 2012, **68**, m165.
- 12 F. H. Allen, O. Kennard, D. G. Watson, L. Brammer, A. G. Orpen and R. Taylor, *J. Chem. Soc., Perkin Trans. 2*, 1987, S1.
- 13 T. Steiner, *Angew. Chem., Int. Ed.*, 2002, **41**, 48.
- 14 M. A. Spackman and D. Jayatilaka, *CrystEngComm*, 2009, **11**, 19.
- 15 M. A. Spackman and J. J. McKinnon, *CrystEngComm*, 2002, **4**, 378.
- 16 S. K. Wolff, D. J. Grimwood, J. J. McKinnon, M. J. Turner, D. Jayatilaka and M. A. Spackman, University of Western Australia, 2012.
- 17 (a) G. te Velde, F. M. Bickelhaupt, E. J. Baerends, C. Fonseca Guerra, S. J. A. van Gisbergen, J. G. Snijders and T. Ziegler, *J. Comput. Chem.*, 2001, **22**, 931 and references therein; (b) E. J. Baerends, J. Autschbach, D. Bashford, A. Bérces, F. M. Bickelhaupt, C. Bo, P. M. Boerrigter, L. Cavallo, D. P. Chong, L. Deng, R. M. Dickson, D. E. Ellis, M. van Faassen, L. Fan, T. H. Fischer, C. Fonseca Guerra, A. Ghysels, A. Giammona, S. J. A. van Gisbergen, A. W. Götz, J. A. Groeneveld, O. V. Gritsenko, M. Grüning, F. E. Harris, P. van den Hoek, C. R. Jacob, H. Jacobsen, L. Jensen, G. van Kessel, F. Kootstra, M. V. Krykunov, E. van Lenthe, D. A. McCormack, A. Michalak, M. Mitoraj, J. Neugebauer, V. P. Nicu, L. Noodleman, V. P. Osinga, S. Patchkovskii, P. H. T. Philipsen, D. Post, C. C. Pye, W. Ravenek, J. I. Rodríguez, P. Ros, P. R. T. Schipper, G. Schreckenbach, M. Seth, J. G. Snijders, M. Solà, M. Swart, D. Swerhone, G. te Velde, P. Vernooijs, L. Versluis, L. Visscher, O. Visser, F. Wang, T. A. Wesolowski, E. M. van Wezenbeek, G. Wiesenekker, S. K. Wolff, T. K. Woo, A. L. Yakovlev and T. Ziegler, *Theoretical Chemistry*, Vrije Universiteit, Amsterdam.
- 18 (a) T. Ziegler and A. Rauk, *Theor. Chim. Acta*, 1977, **46**, 1; (b) M. Mitoraj and A. Michalak, *J. Mol. Model*, 2007, **13**, 347; (c) M. P. Mitoraj, A. Michalak and T. Ziegler, *J. Chem. Theory Comput.*, 2009, **5**, 962.
- 19 SADABS, Bruker AXS Inc., Madison, Wisconsin, USA, 2008.
- 20 G. M. Sheldrick, *Acta Crystallogr., Sect. A: Fundam. Crystallogr.*, 2008, **64**, 112.
- 21 G. M. Sheldrick, *SHELXL2014/7*, University of Göttingen, Germany, 2014.
- 22 C. B. Hübschle, G. M. Sheldrick and B. Dittrich, *J. Appl. Crystallogr.*, 2011, **44**, 1281.
- 23 Rigaku Oxford Diffraction, *CrysAlisPro Software system, Version 1.171.37.31*, Rigaku Corporation, Oxford, UK, 2014.
- 24 I. J. Bruno, J. C. Cole, P. R. Edgington, M. Kessler, C. F. Macrae, P. McCabe, J. Pearson and R. Taylor, *Acta Crystallogr., Sect. B: Struct. Sci.*, 2002, **58**, 389.